

Structural and Electrical Characterizations of BiSb Topological Insulator Layers Epitaxially Integrated on GaAs

Dima Sadek, Richard Daubriac, Corentin Durand, Richard Monflier, Quentin Gravelier, Arnaud Proietti, Fuccio Cristiano, Alexandre Arnoult, Sébastien Plissard

▶ **To cite this version:**

Dima Sadek, Richard Daubriac, Corentin Durand, Richard Monflier, Quentin Gravelier, et al.. Structural and Electrical Characterizations of BiSb Topological Insulator Layers Epitaxially Integrated on GaAs. Crystal Growth & Design, 2022, 22 (8), pp.5081-5091. 10.1021/acs.cgd.2c00585 . hal-03775836

HAL Id: hal-03775836
https://laas.hal.science/hal-03775836

Submitted on 16 Sep 2022

HAL is a multi-disciplinary open access archive for the deposit and dissemination of scientific research documents, whether they are published or not. The documents may come from teaching and research institutions in France or abroad, or from public or private research centers.

L'archive ouverte pluridisciplinaire **HAL**, est destinée au dépôt et à la diffusion de documents scientifiques de niveau recherche, publiés ou non, émanant des établissements d'enseignement et de recherche français ou étrangers, des laboratoires publics ou privés.

Structural and electrical characterizations of BiSb topological insulator layers epitaxially integrated on GaAs

Dima Sadek [1], Richard Daubriac [1], Corentin Durand [1], Richard Monflier [1], Quentin Gravelier [1], Arnaud Proietti [2], Fuccio Cristiano [1], Alexandre Arnoult [1], Sébastien R. Plissard [1,]*

1 - LAAS-CNRS, Université de Toulouse, CNRS, UPS, F-31400 Toulouse, France
2 - Centre De Microcaractérisation Raimond Castaing, Espace Clément Ader, 3 Rue Caroline Aigle, F-31400 Toulouse France

* *To whom correspondence should be addressed.*
E-mail: sebastien.plissard@laas.fr

KEYWORDS: Topological Insulator – Bismuth – Antimony – Chalcogenide – GaAs

ABSTRACT:

Topological insulators (TIs) are known as promising materials for new nanoelectronics and spintronics applications thanks to their unique physical properties. Among these TIs, the Bismuth Antimony alloys ($Bi_{1-x}Sb_x$) remain the most interesting because the electronic band structure can be controlled by changing the stoichiometry, the thickness or the temperature. However, integrating this material on an industrial substrate remains a challenge. Here, we investigate the growth, the structural and the electrical properties of BiSb materials epitaxially deposited on industrial GaAs(001) substrates. We report the influence of key growth parameters such as temperature, antimony composition, thickness and growth rate on the crystal quality. We manage to optimize the growth conditions while keeping the $Bi_{1-x}Sb_x$ composition within the TI range. Despite the large lattice mismatch and the different crystalline matrices between the deposited material and the substrate, we successfully grow high-quality BiSb(0001) films. For optimized growth conditions, a n-type semiconductor behavior of the BiSb layer is demonstrated at temperatures above *100 K*. The material bandgap calculated from our transport measurements corresponds to that mentioned in the literature. A change of the carrier type from bulk electrons to surface holes is observed when decreasing the temperature below *55K*. Hole mobilities up to *7620 cm²/V.s* are extracted. This is to our knowledge the first demonstration of TI integrated on an industrial substrate keeping its protected surface states.

TEXT:

1. Introduction

Topological insulators (TIs) are a new class of materials that were developed over the last fifteen years and have great potential for Quantum Computers and Spintronics applications[1,2]. This new phase of matter is characterized by an inverted bulk bandgap driven by strong spin-orbit interactions. As a direct result, the TI surface exhibits metallic states topologically protected from the environment[3] thanks to the combination of time-reversal symmetry and spin-orbit interactions[4,5]. Contrary to hybrid semiconductor-superconductor devices[6–9], a TI coupled to a superconductor[10] shows promises for harboring and protecting Majorana bound states[11] against environment and thus building extremely robust quantum bits (Qubits)[12]. Moreover, considering that some TIs have a large spin Hall angle and a high electrical conductivity[13], their coupling to a ferromagnetic material[14,15] induces an efficient spin-transfer torque (STT)[13,14]. This is considered as the qualitative leap in the realization of magneto-resistive random access memories (MRAM)[13].

Since 2007, numerous TIs have been discovered starting with HgTe for 2D TIs[16], Bismuth Antimony ($Bi_{1-x}Sb_x$) alloys for 3D TIs[17] and chalcogenide compounds such as Bi_2Se_3, Sb_2Te_3 and Bi_2Te_3[18]. Nevertheless, $Bi_{1-x}Sb_x$ remains the most interesting one thanks to its high conductivity ($\sim 10^5\ \Omega^{-1}.m^{-1}$)[13] and its colossal spin Hall angle (~ 52)[19]. Furthermore $Bi_{1-x}Sb_x$ is the first 3D TI experimentally confirmed by Hsieh *et al.*[3] after being theoretically predicted by Fu and Kane[20]. In this later paper, authors perform Angle-Resolved PhotoEmission Spectroscopy (ARPES) measurements on a $Bi_{0.9}Sb_{0.1}$

surface and observe metallic surface states crossing the Fermi level an odd number of times along a path connecting two time-reversal-invariant momenta in the same Brillouin zone, a negative Z_2 *(-1)* topological invariant and large spin-orbit interactions. Moreover, they study the evolution of the band structure as a function of the alloy composition and report a TI behavior for an antimony composition ranging from 7 to 22%.

Recent studies have shown that two-dimensional (2D) $Bi_{1-x}Sb_x$ layers are of particular interest due to the possibility to control their electronic band structure by changing the film thickness, its composition and the growth direction[21]. It is thus possible to define a variety of Dirac cones at the surface of a $Bi_{1-x}Sb_x$ thin film[2]. Despite numerous studies reporting the growth of BiSb materials[11,15,22,23], the integration of high-quality thin films on industrial substrates remains challenging due to large lattice mismatches, different crystalline matrices and difficult surface preparations. Here, our objective is to integrate $Bi_{1-x}Sb_x$ alloys on an industrial GaAs(001) substrate for nanoelectronics and optoelectronics applications. The BiSb crystalline structure is rhombohedral (R-3m), while that of GaAs(001) is cubic and the lattice mismatch between both is 13,7%. To our knowledge, only three papers report the synthesis of a BiSb layer on GaAs(001), including our previous study[24]. In the first one[13], BiSb(012) layers are obtained on GaAs(001) after deposition of a 3 nm-thick MnGa layer (a ferromagnetic layer) but no information is revealed on the sample quality. In the second study[22], authors try to grow BiSb directly on GaAs(001) and obtain a textured BiSb thin film.

Here we investigate the direct integration of high quality BiSb layers on industrially available GaAs(001) substrates using a MBE412 RIBER molecular beam epitaxy (MBE) system. We study the effect of the growth conditions such as temperature, stoichiometry, film thickness and growth rate on the structural quality on the BiSb layer. Finally, we demonstrate the excellent electronics properties of such TI materials directly integrated on GaAs(001).

2. Method:

$Bi_{1-x}Sb_x$ thin films are grown on 2 inches undoped GaAs(001) wafers from AXT in our MBE system. Once the wafers are loaded into the MBE cluster system and that the ultra-high vacuum (UHV) is reached, they are transferred into the preparation chamber for degassing at 300°C for 1 hour. They are then loaded in the growth chamber, which is equipped with a 20kV STAIB reflection high energy electron diffraction (RHEED) set up. Prior to growth, atomic fluxes (atomic beam equivalent pressures) are calibrated using a Bayard-Alpert Gauge. For all the samples, the Ga and As fluxes are chosen in order to obtain a V/III ratio of 2 and the Sb and Bi fluxes are adapted for each samples. The substrate temperature is probed by both a thermocouple and a band edge measurement (BandiT from kSA). In the following, only "real" temperatures (T_r) measured by BandiT are reported. The correspondence between BandiT temperatures and the thermocouple ones is given in **figure SI-1**. The substrate temperature (*Tr*) is gradually increased from 100 to 635°C under an As flux of 1.2×10^{-5} Torr for temperatures above 400°C. The wafer is deoxidized at 635°C for 10 min and then the temperature is cooled down to 580°C to grow a 1µm-thick GaAs buffer layer with a V/III ratio of 2 in 1 hour. Next, the temperature is cooled down to the BiSb growth

temperature by keeping the same arsenic flux on (1.2×10^{-5} Torr) for temperature above 400°C. According to RHEED records, the change in temperature leads to the GaAs(001) surface reconstruction transitioning from $\beta_2(2\times4)$ to $c(4\times4)$ when the temperature is below 505°C[25]. Finally, after temperature stabilization the BiSb growth is initiated (terminated) by opening (closing) simultaneously the Bi and Sb shutters. The BiSb thickness and composition are determined by X-Ray diffraction (XRD) in a Bruker D8-Discover diffractometer and the surface morphology characterized by Scanning Electron Microscopy (SEM, FEI Aztec-600i) and Atomic Force Microscopy (AFM). Further Electron Back Scattering Diffraction (EBSD) measurements are carried out in a FEG-SEM JEOL JSM 7100F equipped with a Nordlys Nano EBSD camera (Oxford Instruments) in order to obtain an EBSD map and EBSD-pole figures of the samples. XRD-pole figures are obtained using the Bruker D8-Discover diffractometer. Finally, Hall measurements are performed in order to investigate the electronic properties of BiSb films.

3. Results and Discussion:

3.1 The influence of temperature

The initial growths are performed in order to find the optimum temperature window to grow $Bi_{1-x}Sb_x$ films on GaAs(001) substrates with x being in the TI range. Five 250 nm thick layers are thus grown with an antimony composition of 10% and growth temperatures (T_r) of *132, 144, 155, 166* and *177°C* (thermocouple temperatures of *180, 200, 220, 240* and *260°C* respectively). The Bi and Sb fluxes are 4.5×10^{-7} Torr and 5×10^{-8} Torr, respectively. Scanning Electron Microscopy (SEM) images of these

samples are presented in **figure 1**. It shows that the growth is polycrystalline and that the surface morphology is directly dependent on the temperature. For T_r = *132°C* (**Figure 1a**), the surface is rough and has a large number of misoriented grains. Increasing the temperature (**figures 1b,c**) decreases the surface roughness, increases the grain size and optimizes their orientations: more grains present a flat top facet for T_r = *155°C*. However, increasing the temperature further (**figures 1d,e**) worsens the situation: the density of misoriented grains increases and holes appear in the BiSb film. This can be explained by an evaporation of bismuth adatoms from the substrate surface due to its low saturation vapor pressure. **Figure 1f** clearly shows the effect of high temperature (T_r = *177°C*): the red arrow highlights a BiSb droplet that was evaporated after being absorbed at the substrate surface. The melting point of the BiSb system under UHV seems to be around T_r = *177°C*, lower than that calculated at the atmospheric pressure (*~271°C*, see **Supp. Inf. figure SI-2**). According to this series, a growth window around *155°C* is favored in order to achieve a high crystallinity of $Bi_{0.9}Sb_{0.1}$ films.

In order to investigate the in-plane epitaxial relationship between the BiSb layer and the GaAs(001) substrate and to probe the temperature dependence of the BiSb texture, XRD pole figure measurements were carried out (see **figures 2**). For reference, the pole figure of the GaAs(001) substrate taken at the Bragg diffraction angles of the BiSb(0006) is presented in **figure 2a.** It can be noticed that no peak is present at Ψ*=0°*, and that {011}, {112}, {113}, {311} diffraction peaks are observed with a typical square geometry. **Figures 2b-f** present the stereographic projection of BiSb films. All these figures are obtained at $\theta \sim 23°$ corresponding to the (0006) planes of the BiSb layers.

The x axis corresponds to the $[110]$ direction and y axis to the $[\bar{1}10]$ one. First in **figures 2b-f**, the central peak, corresponding to *Ψ=0°*, has a strong intensity, which demonstrates a preferential $[0001]$ growth direction of the BiSb layer. Moreover, all diffraction spots detected in the reference pole figure are also observed at the same position in **figures 2b-f** giving evidence that the BiSb(0001) does not present any rotation with respect to the GaAs(001) substrate: $[11\bar{2}0]_{BiSb} = [110]_{GaAs}$. This is in good agreement with the theoretical model reported in the **Supporting Information figure SI-3** and our previous study[24]. Interestingly, the central peak is elongated along the [110] direction for all $Bi_{0.9}Sb_{0.1}$ samples (**figures 2 b-e**) except the one grown at T_r = *177°C* (**Figure 2f**). This indicates a [110] anisotropic tilt direction for temperatures below *166°C*. For $Bi_{0.9}Sb_{0.1}$ films grown at *Tg = 132°C*, the intensity is distributed over the entire pole figure (**figure 2b**) indicating that the grains orientations are randomly distributed. On the contrary, increasing the temperature to *144°C* leads to a focus of peak intensities at specific Ψ angles and the appearance of axiotaxial rings[26]. This indicates that the surface is starting to organize but still presents an axiotaxial texture and misoriented grains. No more rings are visible and spots are more intense at T_r = *155°C*, which highlights a good crystalline arrangement and surface organization. Finally, axiotaxial rings appear again for temperatures above *166°C* indicating an increase of the misoriented grain density in different direction. For T_r = *177°C*, the partial disappearance of the central peak shows the loss of the (0001) preferential growth orientation.

3.2 The influence of the composition:

After a fine tuning of the growth temperature to $T_r = 151°C$ in order to reduce the surface roughness, we worked on the antimony composition of the BiSb layer. Four 250 nm thick samples were grown by keeping a Bi flux of 4.5×10^{-7} Torr and adapting the Sb one for compositions of 5, 10, 15 and 20%. Interestingly, the final composition of the BiSb layer, measured by XRD, corresponds roughly to the beam equivalent pressure (BEP) ratio of each element. Consequently, Sb fluxes of 2.26×10^{-8}, 5.00×10^{-8}, 7.94×10^{-8} and 11.25×10^{-8} Torr are used for composition of 5%, 10%,15% and 20% respectively.

The surface morphology of the $Bi_{0.95}Sb_{0.05}$, $Bi_{0.9}Sb_{0.1}$, $Bi_{0.85}Sb_{0.15}$ and $Bi_{0.8}Sb_{0.2}$ samples is shown in **figures 3b,c,e** and **f** respectively. It can be noticed that in the case of a low Sb composition (5%), the surface is rougher, disorganized and has a large number of holes compared to other samples. On the opposite, when the Sb composition is 10%, the surface morphology becomes organized due to the nucleation of a great number of grains having a flat top facet. It can be noticed additionally that some grains have a triangular shape pointing upward (see the red triangles) or downward (see the black triangles) in the $[\bar{1}10]$ direction. This indicates a good epitaxial relationship between BiSb films and GaAs(001) substrate. Finally, increasing further the Sb composition (15 and 20%) leads to an increase in the misoriented grain density and to the appearance of holes which affect the BiSb films quality. This trend proves the necessity to adapt the growth temperature to the Sb composition. Feutelais *et al.*[27] have shown that the phase diagram of Bismuth-Antimony alloys exhibits a continuous solid solution phase (Supporting Information **figure SI-2**), which is strongly affected by the Sb composition. More antimony yields to an increase of the melting point and therefore change the optimal growth temperature.

To assess the relationship between the composition (x) and the growth temperature (T_g), $Bi_{0.95}Sb_{0.05}$ and $Bi_{0.85}Sb_{0.15}$ samples were grown at *141°C* and *163°C* respectively (**figures 3a,d**). Interestingly the surface morphology of these samples is totally different from those grown at *151°C* for the same Sb compositions: they are smoother and better organized. The BiSb alloy quality therefore strongly depends on the x and T_r combination: $Bi_{0.95}Sb_{0.05}$ is optimized around *141°C*, $Bi_{0.9}Sb_{0.1}$ at *151°C* and $Bi_{0.85}Sb_{0.15}$ has a better surface morphology at *163°C*. Consequently, increasing the composition must be accompanied by an increase of the growth temperature in order to achieve high crystallinity.

In our previous article[24], electron backscattering diffraction (EBSD) measurements were carried out on the four samples grown at T_r = *151°C* and confirmed the high crystallinity of the $Bi_{0.9}Sb_{0.1}$ film since it has more than 80% of grains having a negligible tilt (lower than 5°) with respect to the substrate (Supporting Information **figures SI-4a-d**). Moreover, a Sb composition dependence of the grain orientation was directly detected; increasing antimony promotes a grain tilting around 10°, while it is between 20 and 35° for low antimony compositions (Supporting Information **figure SI-4e**). Interestingly, there is a link between the grains size and their orientation: the more negligible their tilt, the larger they are (Supporting Information **figure SI-4f**). Indeed, grains having a flat top facet overgrow laterally until they develop enough and coalesce. On the other hand, some misoriented grains keep developing while others disappear and merge with flat top-faced grains. The BiSb nucleation mechanism will be further discussed in the following section.

In order to probe the influence of the Sb composition on the grain tilting direction, pole figures obtained from EBSD measurements were analyzed on these samples. **Figures 4** shows the {0001} EBSD pole figures where the x axis corresponds to the $[110]$ direction and the y axis to the $[\bar{1}10]$ one. It can be noted that the grain tilting directions depend on the Sb composition. For a Sb composition of 5% (**figures 4a**), the grains having a tilt lower than 40° present two preferential tilt direction, the $[100]$ or $[010]$ ones. Moreover, grey spots of unknown orientation are observed and form a 45° tilt square. On the contrary, for a Sb composition greater than 5%, the grains tilt direction is distributed uniformly in either the $[110]$ or the $[\bar{1}10]$ directions (**figures 4b-d**). These results reveal that more antimony (≥10%) improves the grain nucleation mechanism, which promotes uniformity in grain tilt distribution. They also make it possible to deduce that reducing the Sb composition to 5% with T_r = *151°C* leads to a rotation of the BiSb layer of 45° with respect to the GaAs(001) substrate $[10\bar{1}0]_{Bi_{0.95}Sb_{0.05}} = [110]_{GaAs}$. Finally, to define grain orientation indexed in grey, $\{10\bar{1}0\}$, $\{11\bar{2}0\}$, $\{1\bar{1}02\}$ and $\{1\bar{1}0\bar{1}\}$ pole figures were taken for the four samples (Supporting Information **figures SI-5, 6, 7 and 8**). Regardless of the composition, no specific grain orientation is observed.

3.3 <u>The influence of the thickness:</u>

To further investigate the growth mode, a thickness series was synthesized. Six samples of different thicknesses ranging from 2 to 450 nm are grown under the same conditions. The $Bi_{0.9}Sb_{0.1}$ growth is initiated by opening both Bi and Sb shutters at the same time with a flow of 4.5×10^{-7} and 5×10^{-8} Torr, respectively. The growth temperature

is fixed at *151°C* and the growth is terminated once the sample thickness is established. After growth, AFM, SEM and Hall measurement are carried out on these samples.

Figures 5a-f show AFM images of different $Bi_{0.9}Sb_{0.1}$ thin films having a thickness of 2, 20, 30, 60, 90 and 450 nm, respectively. At the early stage of growth (2 nm), different islands can be observed at the substrate surface (**figure 5a**), which indicates a Volmer Weber growth mode. These islands will expand over time and merge with neighbors ones to form bigger grains as observed for the 20 nm thick layer (**figure 5b**). Once a critical density is achieved, for sample thicknesses above 30 nm, the grains develop, become larger and coalesce leading to the formation of a continuous layer (**Figures 5c-f**). In order to define a critical thickness, corresponding to the grain coalescence, an in-situ optical monitoring of the wafer curvature was carried out on the 90 nm thick sample[28]. This measurement records the accumulated stress during the BiSb growth (see **figure SI-9**). At the beginning of the BiSb growth, a compressive stress appears on the wafer corresponding to the grain nucleation. After a ~ *12 nm* growth, the compressive strain change into a tensile one, which corresponds to the coalescence of small islands as confirmed in **figures SI-10a,b**. Finally, after 30 nm, the accumulated stress reaches a plateau when the interconnected grains start forming a continuous network, slowly transforming into a continuous layer (**figures 5c-f**). Importantly, the larger the thickness, the larger the grains with a flat upper facet. Initially for a thickness of 2 nm, the grains seem to have almost the same size and have an homogenous arrangement on the substrate (see **figures 5a** and **SI-10a**). However, this distribution becomes a little less homogenous by increasing the sample thickness to 10-20 nm (see **figures 5b** and **SI-10b,c**), where some grains develop and other disappear.

These results indicate that the larger the grains, the more stable they are since they minimize their surface energy. As a result, the adatoms on the substrate surface and even the small grains tend to migrate and merge with the larger grains, causing them to grow and some existing small ones to disappear.

Starting from 30nm, corresponding to **figures 5c** and **SI-10d**, adatoms accumulate around the flat-topped grains, which lead to their lateral overgrowth and finally to their coalescence with neighbors leading to the creation of a continuous layer. These results confirm that our $Bi_{1-x}Sb_x$ growths are controlled by thermodynamics rather than kinetics: it is favorable for adatoms to stick to an existing island compared to nucleate a new one. Small islands are desorbed and absorbed by bigger ones. In order to favor this mechanism and grow large and flat grains, the kinetics of the system should be slowed down to promote thermodynamics (see following section). Moreover, it is worth mentioning that hexagonal shape grains are observed in **figure 5a** confirming a (0001) growth direction from nucleation.

3.4 The influence of the kinetics on the growth:

In order to probe further the growth mechanisms of the BiSb layer, four samples with a Sb composition of 10% were synthesized with different growth rates and a total layer thickness of *200 nm*. Once the sample temperature is stabilized at *151°C*, the Bi and Sb shutters are opened simultaneously for different growth rates of *0.064 µm/h, 0.129 µm/h, 0.26 µm/h* and *0.385 µm/h* and closed simultaneously after *200 min*, *100 min*, *50 min* and *30 min*, respectively. At this growth temperature, the BiSb system is in

stable phase according to the BiSb phase digram[29], which means that the evaporation rate is almost zero. A SEM imaging of these samples is reported in **figure 6**.

It can be noticed that a high growth rate favors islands growth (**figure 6a**) whereas a low growth rate favors 2D layers growth (**figure 6d**). As a result, the surface morphology for a high growth rate is less organized and presents more misoriented grains (**figure 6a**) compared to a low growth rate (**figure 6d**). This can be explained by thermodynamics and kinetics considerations. Indeed, the adatoms density (n) at a time t and the mean time interval (Δt) between the atoms arrival at the substrate surface will change with the growth rate. When the growth rate increases, n increases while Δt decreases and reciprocally. A large Δt (low growth rate) indicates a high probability that an adatom will reach its thermodynamics equilibrium and stick to an existing island. As consequence, low energy islands, i.e. flat-topped grains in our system, are favored while decreasing the growth kinetics. They will therefore attract a larger number of adatoms if the growth rate decreases, so that their lateral size increases. In the extreme case of a very low growth rate (**Figure 6d**), a continuous layer of flat-topped grains is achieved leading to an optimized surface morphology of the BiSb layer and improved electrical properties.

3.5 The BiSb electronic properties:

Now that the structural and morphological characteristics of the BiSb layers are optimized for integration on an industrial substrate, we focus on their electrical properties. Three $Bi_{0.9}Sb_{0.1}$ samples of *60 nm*, *450 nm* and *1 µm* thicknesses are grown at *151°C* using Bi and Sb fluxes of 4.5×10^{-7} and 5×10^{-8} Torr, respectively. Samples are

then prepared for electrical characterizations using the fabrication processes described in Supporting Information (**figure SI-11**). The electronic properties of BiSb layers were studied following the van der Pauw method. First, the sample sheet resistance R_s is extracted from standard four-point-probe measurement (4PP). The Hall coefficient R_H is then measured using an external magnetic field of 0,3 Tesla orthogonal to the sample's surface. From these two parameters, we can calculate the Hall sheet concentration N_H and the Hall mobility μ_H.

Figure 7a shows the evolution of the sheet resistance in ohm per square (R_s) as a function of the sample thickness at room temperature. For a *20 nm* deposition or below (blue squares in **Figure 7a**), the samples exhibit a high sheet resistance. As mentioned before, these thicknesses correspond to BiSb materials forming small isolated grains rather than a continuous layer. In these conditions, the current is carried through the GaAs substrate rather than in the BiSb grains, which explains the measured sheet resistance of $R_s \sim 10^7 \Omega/\square$ close to the substrate one (*~5×10^{7}Ω/□*). At 30 nm, the sheet resistance drops quickly since the critical layer thickness is reached. The transition observed in the sheet resistance corresponds to the observed beginning of coalesce of small grains into large interconnected domains (see **figure 5** and **SI-10**), opening thus a new channel with a higher conductance. Further increase of the thickness does not increase the size of these domains and leads to a continuous layer (≥ *90 nm*) with much lower sheet resistance, down to $2.3\ \Omega/\square$ for a *1 µm* thick layer.

Assuming that the current flowing through the GaAs substrate is negligible for thicknesses of 60 nm and beyond, we calculated the resistivities (ρ_f) from the corresponding sheet resistance values and the BiSb layers thicknesses. It appears that

the resistivity is thickness dependent as shown in **figure 7b**. Based on an extended version of the Fuchs-Sondheimer model[30–32] predicting the electrical properties inside polycrystalline layers, we extracted an electron mean free path l_g about *265 nm* which is better than the one reported in the literature[33–35] (~ *150 nm*).

In this model, the thin film resistivity is given by:

$$\rho_f = \rho_0 \left[1 + \frac{3}{8t}(1-p) l_0\right] \qquad (1)$$

where ρ_0 and l_0 are respectively the bulk crystal resistivity and mean free path, t the thickness and *p* the probability of carriers being scattered at the surface. In the case of a polycrystalline thin film, Tellier *et al*.[32] showed that **equation 1** remains valid when using ρ_g , the hypothetical polycrystal bulk resistivity, instead of ρ_0 and substituting l_0 by an effective mean free path l_g defined by: $l_g \approx \frac{\rho_0}{\rho_g} l_0$. The validity of this model is restricted by grains and boundaries being identical for the different thicknesses and by the t/l_0 ratio being greater than 0,6[32]. In our case, these conditions are verified for layer thicknesses greater than *90 nm* (see red diamonds in **figure 7b**). In our calculations, we assume that all charge carriers are diffusely scattered at the surface, which means that *p*, the probability that carriers are specularly reflected at the layer surface, is considered zero and that the calculated value for l_g is minimized (for *p = 0,5* the value of l_g is doubled).

Figure 7c shows the evolution of the sheet resistance R_s as a function of the temperature for the *60 nm*, *450 nm* and *1 µm* thick samples. For the three thicknesses, the sheet resistance R_s increases as the temperature decreases (starting at *T = 300 K*), indicating the semiconductor behavior of the BiSb film. The *60 nm* curve reaches a plateau for *T < 100 K*. The *450 nm* and *1 µm* ones both exhibit a transition around *55 K*.

Below this temperature, R_s saturates for the *450 nm* thick sample and starts decreasing for the *1 µm* one. These trends, together with the analysis of the carrier mobility values that will be presented in the following, are consistent with metallic surfaces states on topological insulators as published in many studies[36]. **Figure 7d** shows that $\ln(\rho)$ has a linear dependence with $1/T$ for temperatures above the aforementioned transition. This Arrhenius plot of the resistivity ρ indicates a thermally activated behavior. From the slope of the linear fit, we extracted an activation energy for the different thicknesses: *15,4 meV* for a *1 µm* thick sample, *17,7 meV* for the *450 nm* one and *18,0 meV* for the *60 nm* one. These activation energies are of comparable values to the mid-BiSb bandgap energy indicated in the literature[29], which confirms the non-intentionally doped (NID) semiconductor behavior of our BiSb bulk materials.

The understanding of the electrical properties of the BiSb layers can be pursued by analyzing Hall parameters values. One must consider that only pure Hall values will be analyzed since the Hall scattering coefficient r_H of BiSb is unknown. **Figure 8** shows the temperature dependence of **(a)** the Hall coefficient R_H, **(b)** the Hall carrier concentration C_H, **(c)** the absolute value of the Hall sheet carrier concentration N_H below the transition temperature and **(d)** the Hall charge carrier mobility μ_H. The first striking feature is that R_H changes sign from negative to positive at *55K* for the *450 nm* and *1 µm* thick samples (**figure 8a**). At high temperature, R_H is negative (electrons are majority carriers), but when decreasing the temperature, it shows an abrupt transition towards positive values (holes are majority carriers). This transition occurs at the same temperature than the one observed in **figure 7c** and is consistent with a transition from a bulk to a surface conduction regime (as explained in the following). For the 60 nm

thick sample, R_H remains negative over the whole temperature range, exhibiting a different behavior than thicker layers. For all samples and in the high temperature range, carriers are thermally activated, as expected for NID semiconductors, and their concentration decreases while decreasing temperature (**figure 8b**). At *300K*, the carrier concentrations per volume of the three samples are in the same order of magnitude (*3-9x10^{19} cm^{-3}*, **table 1**), indicating a similar bulk behavior. On the contrary, below *55K* a distinction between thick (*450 nm* and *1 µm*) and thin (*60 nm*) samples is noticeable in **figure 8c**. Considering a possible conduction channel at the surface, due to gapless surface states, one cannot consider anymore the carrier concentration per volume at low temperature. Thus, the absolute value of the Hall sheet carrier concentration N_H is reported in **figure 8c**. A clear divergence, about one order of magnitude, is visible between thick (*450 nm*, *1 µm* and thin (*60 nm*) samples. These results are compatible with a BiSb TI behavior at low temperature and strongly suggest a n-type bulk conduction for all samples at high temperatures (> *100K*), and p-type topological surface states for the *450 nm* and *1 µm* thick samples at low temperatures (< *55K*).

Thickness (*µm*)	$C_H(300K)$ (*cm^{-3}*)	$N_H(20K)$ (*cm^{-2}*)
0.06	8.82x10^{19} (electrons)	2.32x10^{14} (electrons)
0.45	4.72x10^{19} (electrons)	4.90x10^{13} (holes)
1.00	3.37x10^{19} (electrons)	2.70x10^{13} (holes)

Table 1: Hall concentrations at *300K* and Hall sheet concentration at *20K.* The values are extracted from Hall effect measurements performed on $Bi_{0,9}Sb_{0.1}$ layers of different thicknesses.

The evolution of the Hall mobilities as a function of the temperature is reported in **figure 8d** for the three samples. Here again, the distinction between thin and thick samples is clearly visible. For the *450 nm* and *1 µm* samples, the Hall mobilities show a temperature dependence between *100K* and *300K* close to $T^{-1.9}$ and $T^{-2.3}$, respectively. These trends are close to those induced by a phonon scattering of electrons inside the bulk (known to have $T^{-1.5}$ dependence in conventional semiconductor, like silicon[37]). For the thinnest layer, we found a $T^{-0.9}$ dependence between 220K and 300K. The slope lessening from -2.3 to -0.9 with the thickness reduction might be caused by surface scattering enhancement due to a degraded surface morphology.

At low temperature (< *55K*), the electron Hall mobility of the *60 nm* thick sample remains constant around *80 cm²/(V.s)*, which is most probably due to its poor morphology and the presence of structural holes in the BiSb layer (see **figure 5**). On the contrary, a continuous increase of the hole Hall mobility is reported for the thick samples when decreasing the temperature from *55K* to *20K*. The hole mobilities are respectively 1430 cm²/V.s at 16K for the 450 nm thick sample and 7620 cm²/V.s at 22K for the 1 µm one. Adding to this observation the very high hole mobilities (**figure 8d**) makes it reasonable to assume that these surface states are topologically protected, which confirms the high quality of our BiSb layers directly integrated in GaAs(0001). This is in good agreement with the BiSb topological insulator phase on (111) surfaces, for which holelike bands are predicted to have significant contribution to the surface

conduction[3,19]. Finally, it is interesting to note that for temperatures below 55K, a temperature dependence in $T^{-0.4}$ and $T^{-0.6}$ is observed for the hole mobility (see inset in **figure 8d**). This behavior does not correspond to any known scattering mechanism. Further work is needed to elucidate this point.

4. Conclusions:

In this paper, we have investigated the growth of a $Bi_{1-x}Sb_x$ thin film on an As-rich GaAs(001) cubic substrate using a MBE system. We have shown that despite the large mismatch and the different crystalline structure between the epitaxial film and the substrate, it is possible to obtain a high quality BiSb thin film by optimizing the growth conditions. The first crucial step in obtaining an epitaxial BiSb thin film is the substrate surface preparation. Here, the substrate surface was prepared under the As-rich condition with a GaAs growth rate of *1 µm/h* and a *V/III* ratio of 2. Next, we have confirmed the change of the optimal growth temperature as a function of the Sb composition. We report an optimum growth temperature of *151°C* for a Sb composition of *10%* while it is *141°C* for *5%* and *163°C* for *15%*. These results emphasize the need to increase the temperature with increasing the Sb composition in order to obtain high crystallinity. By optimizing the growth conditions, it is possible to obtain more than 80% of grains having a negligible tilt with the substrate. Moreover, we report a Volmer-Weber growth mode of the BiSb layer on the GaAs(001) substrate: first small islands are nucleated on the substrate surface. Grains having a flat-topped facet are favored by decreasing the growth kinetics and after reaching a critical thickness of *~30 nm* the

islands interconnect and form a continuous layer. Furthermore, the semiconductor behavior of the BiSb layer is demonstrated at temperatures above *100 K*. The material bandgap calculated from our Hall measurements corresponds to that mentioned in the literature. A change of the carrier type from bulk electrons to surface holes is observed when decreasing the temperature for thicker samples. In that case, high hole mobilities of *1430 cm²/V.s* and *7620 cm²/V.s* are reported for respectively *450 nm* and *1 µm* thick samples at low temperature. These measurements are in good agreement with the literature and the presence of topologically protected surfaces states. This is to our knowledge the first demonstration of the BiSb topological insulator behavior integrated on an industrial substrate.

ACKNOWLEDGEMENTS:

This study benefited from the support the LAAS-CNRS micro and nanotechnologies platform, member of the French RENATECH network and was carried out in the EPICENTRE common laboratory between Riber and CNRS.

AUTHOR CONTRIBUTION:

D.S. and S.R.P. conceived the project and experiments.
D.S, A.A. and S.R.P grew the samples.
D.S. and C.D. performed the AFM measurements and A.P. the EBSD ones.
The XRD measurements were carried out by D.S. and A.A..
R.D. and Q.G. prepared the samples for Hall effect measurements and carried out the experiments with D.S. R.M. and C.D..
D.S., R.D. C.D. F.C. A.A. and S.R.P. analyzed the measurements and wrote the manuscript with input from all the authors.

FUNDING SOURCES:

This work is funded by the Agence National de la Recherche (ANR) under grant number ANR-17-PIRE-0001 (HYBRID project).

Supporting information:

The Supporting Information is available free of charge at XXX.

The correspondence between thermocouple and BandiT temperatures is provided as well as the theoretical phase diagram of BiSb, the modeling of the pole figure, the EBSD and the stress measurements and the fabrication processes for Hall devices.

Additional information:

The authors declare no competing financial interests.

References:

(1) Moore, J. E. The Birth of Topological Insulators. *Nature* **2010**, *464* (7286), 194–198. https://doi.org/10.1038/nature08916.

(2) Tang, S.; Dresselhaus, M. S. Electronic Properties of Nano-Structured Bismuth-Antimony Materials. *J. Mater. Chem. C* **2014**, *2* (24), 4710–4726. https://doi.org/10.1039/C4TC00146J.

(3) Hsieh D.; Xia Y.; Wray L.; Qian D.; Pal A.; Dil J. H.; Osterwalder J.; Meier F.; Bihlmayer G.; Kane C. L.; Hor Y. S.; Cava R. J.; Hasan M. Z. Observation of Unconventional Quantum Spin Textures in Topological Insulators. *Science* **2009**, *323* (5916), 919–922. https://doi.org/10.1126/science.1167733.

(4) Young, S. M.; Chowdhury, S.; Walter, E. J.; Mele, E. J.; Kane, C. L.; Rappe, A. M. Theoretical Investigation of the Evolution of the Topological Phase of Bi$_2$Se$_3$ under Mechanical Strain. *Phys Rev B* **2011**, *84* (8), 085106. https://doi.org/10.1103/PhysRevB.84.085106.

(5) Hasan, M. Z.; Kane, C. L. Colloquium: Topological Insulators. *Rev Mod Phys* **2010**, *82* (4), 3045–3067. https://doi.org/10.1103/RevModPhys.82.3045.

(6) Hui, H.-Y.; Sau, J. D.; Das Sarma, S. Bulk Disorder in the Superconductor Affects Proximity-Induced Topological Superconductivity. *Phys. Rev. B* **2015**, *92* (17), 174512. https://doi.org/10.1103/PhysRevB.92.174512.

(7) Hui, H.-Y.; Sau, J. D.; Das Sarma, S. Disorder-Induced Subgap States and Majorana Zero-Energy Edge Modes in Two-Dimensional Topological Insulator-Superconductor Hybrid Structures. *Phys. Rev. B* **2014**, *90* (17), 174206. https://doi.org/10.1103/PhysRevB.90.174206.

(8) Chen, J.; Woods, B. D.; Yu, P.; Hocevar, M.; Car, D.; Plissard, S. R.; Bakkers, E. P. A. M.; Stanescu, T. D.; Frolov, S. M. Ubiquitous Non-Majorana Zero-Bias Conductance Peaks in Nanowire Devices. *Phys Rev Lett* **2019**, *123* (10), 107703. https://doi.org/10.1103/PhysRevLett.123.107703.

(9) Su, Z.; Zarassi, A.; Hsu, J.-F.; San-Jose, P.; Prada, E.; Aguado, R.; Lee, E. J. H.; Gazibegovic, S.; Op het Veld, R. L. M.; Car, D.; Plissard, S. R.; Hocevar, M.; Pendharkar, M.; Lee, J. S.; Logan, J. A.; Palmstrøm, C. J.; Bakkers, E. P. A. M.; Frolov, S. M. Mirage Andreev Spectra Generated by Mesoscopic Leads in Nanowire Quantum Dots. *Phys Rev Lett* **2018**, *121* (12), 127705. https://doi.org/10.1103/PhysRevLett.121.127705.

(10) Yu, W.; Niu, C.-Y.; Zhu, Z.; Cai, X.; Zhang, L.; Bai, S.; Zhao, R.; Jia, Y. Strain Induced Quantum Spin Hall Insulator in Monolayer β-BiSb from First-Principles Study. *RSC Adv.* **2017**, *7* (44), 27816–27822. https://doi.org/10.1039/C7RA04153E.

(11) Singh, S.; Romero, A. H. Giant Tunable Rashba Spin Splitting in a Two-Dimensional BiSb Monolayer and in BiSb/AlN Heterostructures. *Phys. Rev. B* **2017**, *95* (16), 165444. https://doi.org/10.1103/PhysRevB.95.165444.

(12) Breunig, O.; Ando, Y. Opportunities in Topological Insulator Devices. *Nat. Rev. Phys.* **2022**, *4* (3), 184–193. https://doi.org/10.1038/s42254-021-00402-6.

(13) Khang, N. H. D.; Ueda, Y.; Hai, P. N. A Conductive Topological Insulator with Large Spin Hall Effect for Ultralow Power Spin–Orbit Torque Switching. *Nat. Mater.* **2018**, *17* (9), 808–813. https://doi.org/10.1038/s41563-018-0137-y.

(14) Mellnik, A. R.; Lee, J. S.; Richardella, A.; Grab, J. L.; Mintun, P. J.; Fischer, M. H.; Vaezi, A.; Manchon, A.; Kim, E.-A.; Samarth, N.; Ralph, D. C. Spin-Transfer Torque Generated by a Topological Insulator. *Nature* **2014**, *511* (7510), 449–451. https://doi.org/10.1038/nature13534.

(15) Fan, T.; Khang, N. H. D.; Nakano, S.; Hai, P. N. Ultrahigh Efficient Spin Orbit Torque Magnetization Switching in Fully Sputtered Topological Insulator and Ferromagnet Multilayers. *Sci. Rep.* **2022**, *12* (1), 2998. https://doi.org/10.1038/s41598-022-06779-3.

(16) Bernevig B. Andrei; Hughes Taylor L.; Zhang Shou-Cheng. Quantum Spin Hall Effect and Topological Phase Transition in HgTe Quantum Wells. *Science* **2006**, *314* (5806), 1757–1761. https://doi.org/10.1126/science.1133734.

(17) Hsieh, D.; Qian, D.; Wray, L.; Xia, Y.; Hor, Y. S.; Cava, R. J.; Hasan, M. Z. A Topological Dirac Insulator in a Quantum Spin Hall Phase. *Nature* **2008**, *452* (7190), 970–974. https://doi.org/10.1038/nature06843.

(18) Zhang, H.; Liu, C.-X.; Qi, X.-L.; Dai, X.; Fang, Z.; Zhang, S.-C. Topological Insulators in Bi2Se3, Bi2Te3 and Sb2Te3 with a Single Dirac Cone on the Surface. *Nat. Phys.* **2009**, *5* (6), 438–442. https://doi.org/10.1038/nphys1270.

(19) Qu, D.-X.; Roberts, S. K.; Chapline, G. F. Observation of Huge Surface Hole Mobility in the Topological Insulator $\mathrmBi_0.91\mathrmSb_0.09$ (111). *Phys Rev Lett* **2013**, *111* (17), 176801. https://doi.org/10.1103/PhysRevLett.111.176801.

(20) Fu, L.; Kane, C. L. Topological Insulators with Inversion Symmetry. *Phys Rev B* **2007**, *76* (4), 045302. https://doi.org/10.1103/PhysRevB.76.045302.

(21) Şahin, C.; Flatté, M. E. Tunable Giant Spin Hall Conductivities in a Strong Spin-Orbit Semimetal: ${\mathrm{Bi}}_{1\ensuremath{-}x}{\mathrm{Sb}}_{x}$. *Phys. Rev. Lett.* **2015**, *114* (10), 107201. https://doi.org/10.1103/PhysRevLett.114.107201.

(22) Yao, K.; Khang, N. H. D.; Hai, P. N. Influence of Crystal Orientation and Surface Termination on the Growth of BiSb Thin Films on GaAs Substrates. *J. Cryst. Growth* **2019**, *511*, 99–105. https://doi.org/10.1016/j.jcrysgro.2019.01.041.

(23) Fan, T.; Tobah, M.; Shirokura, T.; Huynh Duy Khang, N.; Nam Hai, P. Crystal Growth and Characterization of Topological Insulator BiSb Thin Films by Sputtering Deposition on Sapphire Substrates. *Jpn. J. Appl. Phys.* **2020**, *59* (6), 063001. https://doi.org/10.35848/1347-4065/ab91d0.

(24) Sadek, D.; Dhungana, D. S.; Coratger, R.; Durand, C.; Proietti, A.; Gravelier, Q.; Reig, B.; Daran, E.; Fazzini, P. F.; Cristiano, F.; Arnoult, A.; Plissard, S. R. Integration of the Rhombohedral BiSb(0001) Topological Insulator on a Cubic GaAs(001) Substrate. *ACS Appl. Mater. Interfaces* **2021**, *13* (30), 36492–36498. https://doi.org/10.1021/acsami.1c08477.

(25) LaBella, V. P.; Krause, M. R.; Ding, Z.; Thibado, P. M. Arsenic-Rich GaAs(0 0 1) Surface Structure. *Surf. Sci. Rep.* **2005**, *60* (1), 1–53. https://doi.org/10.1016/j.surfrep.2005.10.001.

(26) Detavernier, C.; Özcan, A. S.; Jordan-Sweet, J.; Stach, E. A.; Tersoff, J.; Ross, F. M.; Lavoie, C. An Off-Normal Fibre-like Texture in Thin Films on Single-Crystal Substrates. *Nature* **2003**, *426* (6967), 641–645. https://doi.org/10.1038/nature02198.

(27) Feutelais, Y.; Morgant, G.; Didry, J. R.; Schnitter, J. Thermodynamic Evaluation of the System Bismuth-Antimony. *Calphad* **1992**, *16* (2), 111–119. https://doi.org/10.1016/0364-5916(92)90001-E.

(28) Arnoult, A.; Colin, J. Magnification Inferred Curvature for Real-Time Curvature Monitoring. *Sci. Rep.* **2021**, *11* (1), 9393. https://doi.org/10.1038/s41598-021-88722-6.

(29) Lenoir, B.; Dauscher, A.; Cassart, M.; Ravich, Yu. I.; Scherrer, H. Effect of Antimony Content on the Thermoelectric Figure of Merit of Bi1−xSbx Alloys. *J. Phys. Chem. Solids* **1998**, *59* (1), 129–134. https://doi.org/10.1016/S0022-3697(97)00187-X.

(30) Fuchs, K. The Conductivity of Thin Metallic Films According to the Electron Theory of Metals. *Math. Proc. Camb. Philos. Soc.* **1938**, *34* (1), 100–108. https://doi.org/10.1017/S0305004100019952.

(31) Mayadas, A. F.; Shatzkes, M. Electrical-Resistivity Model for Polycrystalline Films: The Case of Arbitrary Reflection at External Surfaces. *Phys. Rev. B* **1970**, *1* (4), 1382–1389. https://doi.org/10.1103/PhysRevB.1.1382.

(32) Tellier, C. R.; Tosser, A. J.; Boutrit, C. The Mayadas-Shatzkes Conduction Model Treated as a Fuchs-Sondheimer Model. *Thin Solid Films* **1977**, *44* (2), 201–208. https://doi.org/10.1016/0040-6090(77)90455-2.

(33) Osmic, E.; Barzola-Quiquia, J.; Böhlmann, W.; Bercoff, P. G.; Venosta, L.; Häussler, P. Thermopower and Magnetotransport Properties of Bi100−xSbx Topological

Insulator Thin Films Prepared by Flash Evaporation. *J. Phys. Chem. Solids* **2022**, *167*, 110734. https://doi.org/10.1016/j.jpcs.2022.110734.

(34) Taskin, A. A.; Segawa, K.; Ando, Y. Oscillatory Angular Dependence of the Magnetoresistance in a Topological Insulator ${\text{Bi}}_{1\ensuremath{-}x}{\text{Sb}}_{x}$. *Phys. Rev. B* **2010**, *82* (12), 121302. https://doi.org/10.1103/PhysRevB.82.121302.

(35) Taskin, A. A.; Ando, Y. Quantum Oscillations in a Topological Insulator ${\text{Bi}}_{1\ensuremath{-}x}{\text{Sb}}_{x}$. *Phys. Rev. B* **2009**, *80* (8), 085303. https://doi.org/10.1103/PhysRevB.80.085303.

(36) Xu, Y.; Miotkowski, I.; Liu, C.; Tian, J.; Nam, H.; Alidoust, N.; Hu, J.; Shih, C.-K.; Hasan, M. Z.; Chen, Y. P. Observation of Topological Surface State Quantum Hall Effect in an Intrinsic Three-Dimensional Topological Insulator. *Nat. Phys.* **2014**, *10* (12), 956–963. https://doi.org/10.1038/nphys3140.

(37) Stillman, G. E.; Wolfe, C. M. Electrical Characterization of Epitaxial Layers. *Thin Solid Films* **1976**, *31* (1), 69–88. https://doi.org/10.1016/0040-6090(76)90355-2.

FIGURES CAPTIONS:

Figure 1. Secondary electron (SE) SEM images showing the surface morphology of the as-grown $Bi_{0.9}Sb_{0.1}$ layer at a growth temperature T_r of **(a)** 132°C, **(b)** 144°C, **(c)** 155°C, **(d)** 166°C and **(e)** 177°C. The SEM image in panel **(f)** is a zoomed image of the area indicated by the red square in panel **(e)** where adatoms are re-evaporated.

Figure 2. XRD pole figures of different samples using a theta - two theta configuration around the diffraction Bragg angles of the BiSb {0006} planes. A reference measure on a GaAs(001) substrate is provided in **(a)**. The XRD pole figures of the BiSb thin films are reported in **(b)** for a growth temperature of 132°C, in **(c)** for 144°C, in **(d)** for 155°C, in **(e)** for 166°C and in **(f)** for 177°C. The color scale on the right corresponds to the X-Ray diffracted intensity of the samples in a logarithmic scale. Labels near each spot corresponds to the (hkl) planes. All pole figures are performed by rotating the sample around its normal axis (ϕ), at an angular orientation (ψ) of the sample, ranging from 0 to 90°.

Figure 3. Evolution of the BiSb surface morphology as a function of the temperature (T_r) and the Sb composition (x). SEM images of the BiSb layer grown on a GaAs(001) substrate with different compositions **(a)** and **(b)** 5%; **(d)** and **(e)** 15%; **(c)** 10%; **(f)** 20%. The blue, orange and red frames indicate growth temperatures of 141°C, 151°C and 163°C, respectively.

Figure 4. EBSD pole figures of the {0001} planes for different BiSb compositions: **(a)** $Bi_{0.95}Sb_{0.05}$, **(b)** $Bi_{0.9}Sb_{0.1}$, **(c)** $Bi_{0.85}Sb_{0.15}$ and **(d)** $Bi_{0.8}Sb_{0.2}$. The x-axis corresponds to the GaAs [110] direction, whereas it is [-110] for the y-axis. The color scale on the right presents tilt angle ranging from 0 to 40°.

Figure 5. Evolution of the surface morphology as a function of the BiSb layer thickness. The AFM images are taken for thicknessess of **(a)** 2 nm, **(b)** 20 nm, **(c)** 30 nm, **(d)** 60 nm, **(e)** 90 nm and **(f)** 450 nm. Note that holes are present in the BiSb layer for thicknesses below 450nm.

Figure 6. Evolution of the BiSb surface morphology as a function of the growth rate. All layers have the same composition and thickness, and the respective growth rates are: **(a)** 0.385, **(b)** 0.26, **(c)** 0.129 and **(d)** 0.064µm/h.

Figure 7. 4-point-probe measurements on the BiSb layers. **(a)** Evolution of the sheet resistance R_s as function of the BiSb layer thickness t. Blue and red dots refer to non-uniform and continuous grown layers, respectively. **(b)** Evolution of the resistivity with the inverse thickness. Values depicted in red dots fulfill the Tellier *et al.*[32] limitation conditions. The electron mean free path is extracted from the slope of the black straight line. **(c)** Sheet resistance evolution with the temperature for three different BiSb layer thicknesses. **(d)** Calculated values of the resistivity (from R_S) plotted as function of the inverse temperature. The activation energies of the BiSb layers can be extracted from the linear dependences at high temperature, showed in dashed lines.

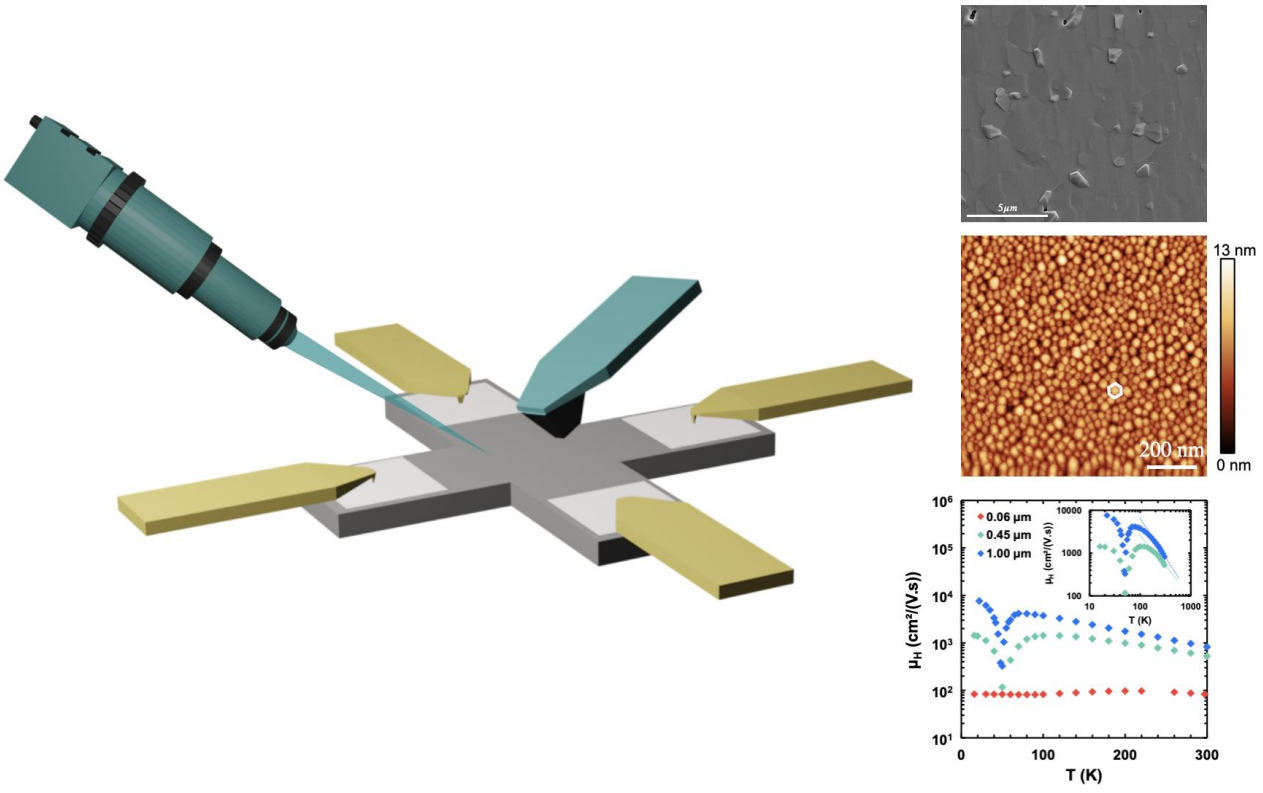
Figure 8. Hall effect measurements on the BiSb layers. **(a)** Evolution of the Hall coefficient R_H, **(b)** the Hall concentration C_H, **(c)** the absolute values of the Hall sheet concentration N_H and **(d)** the Hall mobility μ_H as a function of the temperature. The inset in **(d)** shows the Hall mobility as function of the temperature, in logarithm scales, along with the T^{α} dependencies, in dashed lines.

TOC-Synopsis:

For Table of Contents Use Only

Structural and electrical characterizations of BiSb topological insulator layers epitaxially integrated on GaAs

Dima Sadek [1], Richard Daubriac [1], Corentin Durand [1], Richard Monflier [1], Quentin Gravelier [1], Arnaud Proietti [2], Fuccio Cristiano [1], Alexandre Arnoult [1], Sébastien R. Plissard [1,]*



Characterizations of $Bi_{1-x}Sb_x$ thin films epitaxially integrated on industrial GaAs(001) substrates using a MBE. For this purpose, multiple techniques have been used such as scanning electron microscopy, atomic force microscopy and Hall measurements. All of these techniques demonstrate the growth of a high quality BiSb layer despite large mismatches and different crystalline structures between BiSb and GaAs. They show the growth of a rhombohedral matrix on top of the cubic substrate. In the case of thick samples, a change of the carrier type from bulk electrons to surface holes is reported while decreasing the temperature. This evolution and the high hole mobilities are consistent with topologically protected surface states.